Tunable Plasmonic Nanoparticles with Catalytically Active High-Index Facets

Hao Jing,[†] Qingfeng Zhang,[†] Nicolas Large,[‡] Chunmei Yu,[†,‖] Douglas A. Blom,[§] Peter Nordlander,[‡] and Hui Wang*,[†]

[†]Department of Chemistry and Biochemistry, University of South Carolina, Columbia, South Carolina 29208, United States

[‡]Department of Physics and Astronomy, Department of Electrical and Computer Engineering, Laboratory for Nanophotonics, Rice University, Houston, Texas 77005, United States

[‖]School of Public Health, Nantong University, Nantong, Jiangsu 226019, China

[§]USC Nanocenter, University of South Carolina, Columbia, South Carolina 29208, United States

S *Supporting Information*

ABSTRACT: Noble metal nanoparticles have been of tremendous interest due to their intriguing size- and shape-dependent plasmonic and catalytic properties. Combining tunable plasmon resonances with superior catalytic activities on the same metallic nanoparticle, however, has long been challenging because nanoplasmonics and nanocatalysis typically require nanoparticles in two drastically different size regimes. Here, we demonstrate that creation of high-index facets on subwavelength metallic nanoparticles provides a unique approach to the integration of desired plasmonic and catalytic properties on the same nanoparticle. Through site-selective surface etching of metallic nanocuboids whose surfaces are dominated by low-index facets, we have controllably fabricated nanorice and nanodumbbell particles, which exhibit drastically enhanced catalytic activities arising from the catalytically active high-index facets abundant on the particle surfaces. The nanorice and nanodumbbell particles also possess appealing tunable plasmonic properties that allow us to gain quantitative insights into nanoparticle-catalyzed reactions with unprecedented sensitivity and detail through time-resolved plasmon-enhanced spectroscopic measurements.

KEYWORDS: nanoplasmonics, catalysis, high index facets, surface-enhanced spectroscopy, nanoparticles, tunable plasmon resonances
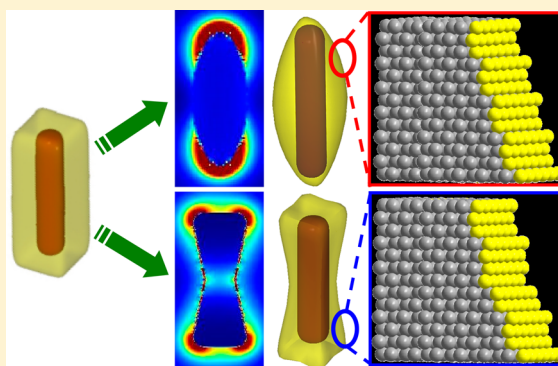
Nanoparticles of noble metals, such as Au, Ag, Pd, and Pt, exhibit intriguing size- and shape-dependent catalytic activities[1−3] and optical properties.[3−5] Although bulk noble metals are considered to be chemically inert, small metal nanoparticles less than 5 nm in diameter have shown remarkable catalytic activities due to the high fraction of undercoordinated surface atoms located at the particle edges and corners.[6−8] Metal nanoparticles show rapid decay in catalytic activity when their sizes increase to beyond ∼10 nm; however, these larger nanoparticles then begin to show geometry-dependent optical properties that are dominated by the collective oscillations of free electrons known as plasmons.[9,10] The capability of fine-tuning the nanoparticle plasmon resonances over a broad spectral range enables widespread applications in photonics,[11] optoelectronics,[12,13] spectroscopies,[14] and biomedicine.[15] Such plasmonic tunability is a unique feature of noble metal nanoparticles in the subwavelength size regime typically from tens of nanometers to submicrometers.[3,5,9,10] For sub-5-nm particles, the plasmon resonances begin to exhibit quantum size effects and the plasmon bands shift and broaden with diminished light scattering and absorption features.[16] Therefore, the combina-

tion of strong, tunable plasmon resonances and superior catalytic activities on the same nanoscale entity remains challenging essentially due to the two drastically different size regimes required for nanoplasmonics and nanocatalysis, respectively.

Our strategy of integrating desired plasmonic and catalytic properties on the same nanostructure is to create high-index facets on subwavelength Ag nanoparticles through controlled nanoscale surface etching. High-index facets exhibit tremendously enhanced catalytic activities in comparison to those close-packed low-index facets because they are open surface structures with a high density of atomic steps, ledges, and kinks, which serve as active sites for breaking chemical bonds.[17,18] Although chemically less stable than Au, Pt, and Pd, Ag nanoparticles offer many advantages for plasmonic applications as they have far stronger plasmon resonances, more intense near-field enhancements, and greater optical tunability than the other noble metal counterparts.[19] The abilities to both
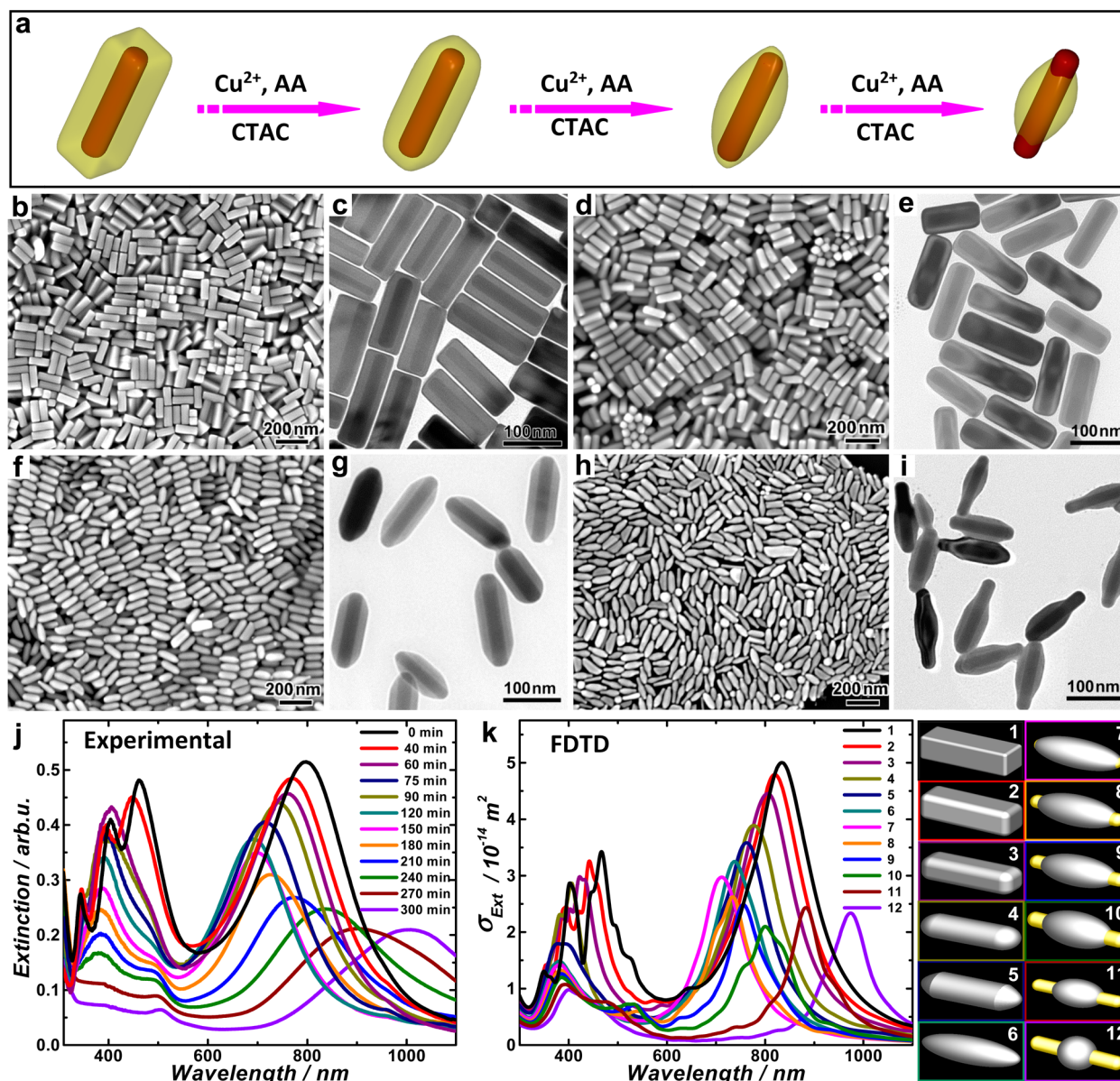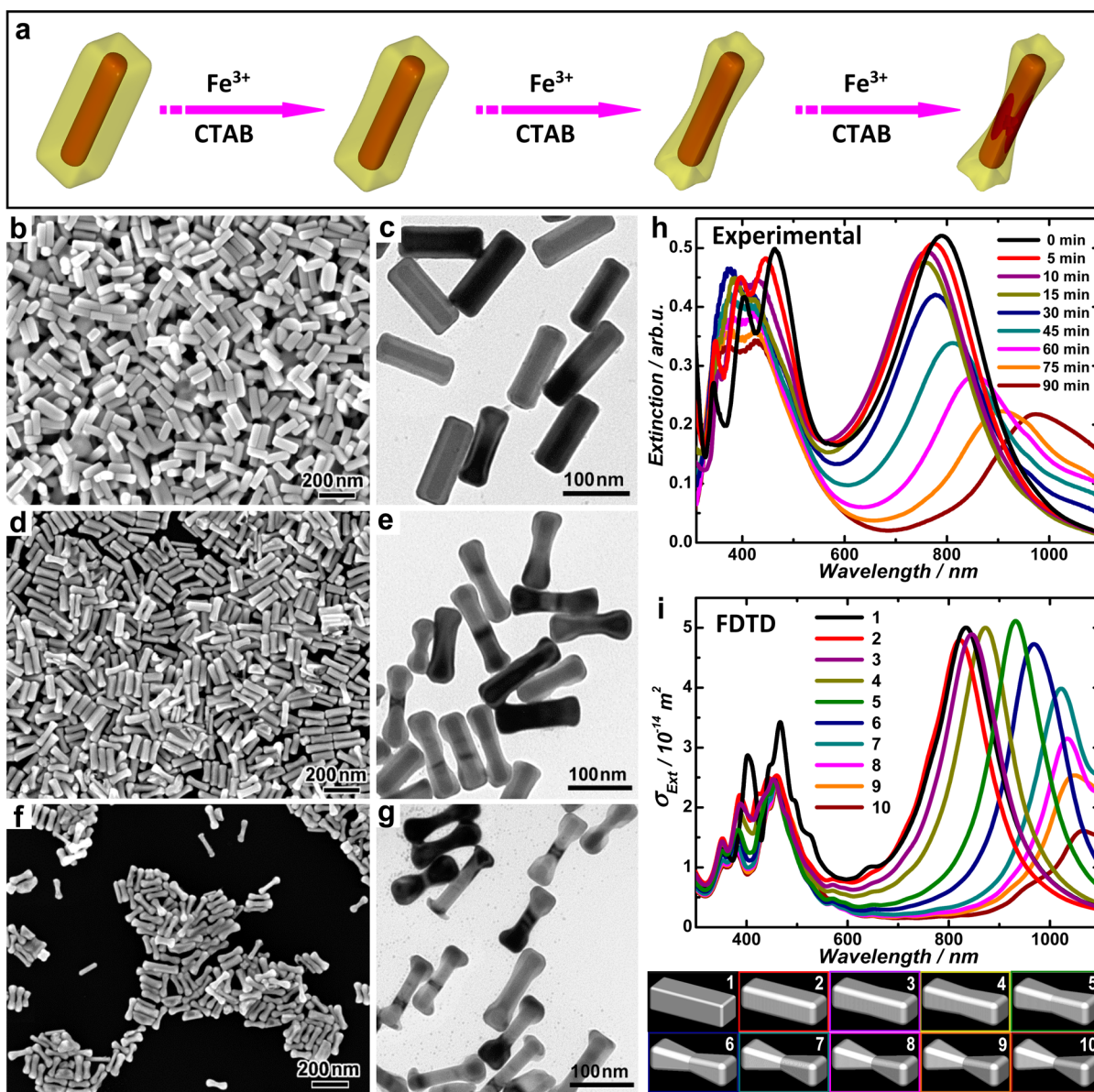
Figure 1. Preferential edge- and corner-etching of Au−Ag core−shell nanocuboids. (a) Schematic illustration of the stepwise morphological evolution of Au−Ag core−shell nanostructures in the presence of CTAC, Cu^{2+}, and AA. SEM and TEM images of (b, c) the nanocuboids and the nanostructures obtained after etching for (d, e) 60 min, (f, g) 120 min, and (h, i) 210 min. Panels b, d, f, and h show the SEM images, and panels c, e, g, and i show the TEM images. (j) Experimental extinction spectra of Au−Ag core−shell nanostructures obtained at different etching times. (k) FDTD calculated extinction spectra showing the spectral evolution during the edge and corner etching of the Au−Ag core−shell nanocuboids. The geometry of the particle being simulated for each extinction spectrum is shown on the right side of panel k.

nanoengineer high-index facets and fine-tune the plasmon resonances of Ag nanoparticles allow one to use these nanoparticles for a dual purpose: as substrates for plasmon-enhanced spectroscopies and as efficient surface catalysts. As demonstrated in this work, such dual functionality opens up unique opportunities for detailed, quantitative study of the kinetics and mechanisms of surface-catalyzed reactions through plasmon-enhanced spectroscopic measurements.

Most of the experimentally realizable noble metal nanoparticles, however, are bound exclusively by low-index facets[20,21] because the high-index facets have higher surface energy and are usually eliminated during the nanocrystal growth.[17] Although synthetically challenging, Au,[22−25] Pt,[17,26−28] Pd,[29,30] and Au−Pd bimetallic[31−34] polyhedral nanoparticles enclosed by various high-index facets have been

recently fabricated through either potential-controlled electrochemical approaches[17,27,29] or facet-controlled nanocrystal growth methods.[22−26,28,30−34] Synthesis of Ag nanoparticles with high-index facets, nevertheless, remains significantly more challenging because of the larger energy differences between the high-index and low-index facets of Ag in comparison to those of the Au, Pd, and Pt.[35] Here we choose Au−Ag core−shell cuboidal nanoparticles, whose surfaces are dominated by the thermodynamically stable low-index {100} facets, as the starting material. By selectively etching the nanocuboid surfaces, we have been able to create catalytically active high-index facets on the particle surfaces in a highly controllable manner while maintaining the capability to fine-tune the nanoparticle plasmons through deliberate geometry control.

Figure 2. Lateral side facet-etching of Au−Ag core−shell nanocuboids. (a) Schematic illustration of stepwise morphological evolution of Au−Ag core−shell nanostructures in the presence of Fe^{3+} and CTAB. SEM and TEM images of the etched nanostructures after etching for (b, c) 10 min, (d, e) 45 min, and (f, g) 75 min. Panels b, d, and f show the SEM images, and panels c, e, and g show the TEM images. (h) Experimental extinction spectra of Au−Ag core−shell nanostructures obtained at different etching times. (i) FDTD calculated extinction spectra showing the spectral evolution during the lateral side facet-etching of the Au−Ag core−shell nanocuboids. The geometry of the particle being simulated for each extinction spectrum is shown at the bottom of panel i.

We used single-crystalline, cylindrical Au nanorods with rounded ends[36] (Figure S1 in the Supporting Information) as the core material. Au−Ag core−shell nanocuboids were then prepared through controlled epitaxial overgrowth of Ag on the Au nanorods.[37] Cetyltrimethylammonium chloride (CTAC) was used as a surface-capping ligand that selectively stabilized the {100} facets of Ag,[38,39] resulting in the formation of Au−Ag core−shell nanocuboids enclosed by six well-defined {100} facets.[37−39] The Ag shell grown on the lateral sides of the Au nanorods was observed to be thicker than that on the ends (see Supporting Information Figures S1c and S2), suggesting a preferential epitaxial growth of Ag on the side facets of the Au nanorods. Energy dispersive spectroscopy (EDS) measurements on individual nanocuboids further confirmed the well-

defined Au core and Ag shell heterostructure (Supporting Information Figure S3).

As schematically illustrated in Figure 1a, the nanocuboids underwent an interesting nanoscale surface-etching process in the presence of Cu^{2+}, ascorbic acid (AA), and CTAC in an aqueous environment at 65 °C, resulting in a gradual morphological evolution from nanocuboids to rice-shaped nanoparticles, and eventually to uncoated Au nanorods. The etching of the nanocuboids was observed to be a continuous process; however, once the particles were separated from the reaction mixture through centrifugation and redispersion in water, the etching was effectively inhibited, allowing us to stop the reaction at any particular etching stage. We used both scanning electron microscopy (SEM) and transmission electron microscopy (TEM) to systematically track the structural

changes of the nanoparticles during the etching process (Figure 1b−i). The Au−Ag core−shell nanocuboids exhibited intrinsic slight truncations at the edges and the corners (Figure 1b and c). The observed morphological evolution during the nanoscale surface-etching process can be interpreted as a result of both the preferential etching of the particle corners and edges by Cu^{2+} and AA and the selective stabilization of Ag {100} facets by CTAC.

Because the plasmonic features of nanoparticles depend sensitively on edge and corner truncations, this morphological evolution could also be monitored by optical extinction spectroscopic measurements (see Figure 1j). Four distinct plasmon peaks at 798, 460, 404, and 342 nm were observed in the extinction spectrum of the colloidal nanocuboids and were assigned to the longitudinal dipole, transverse dipole, and two transverse octupole resonances, respectively.[37] As demonstrated previously, the frequencies and relative intensities of these plasmon resonance modes of the Au−Ag core−shell nano-cuboids are dominated by the geometry of the Ag shell and can be systematically tuned across the visible and near-infrared regions by controlling the aspect ratio of the Au nanorod core or the thickness of the Ag shell.[37−39] Here, the controlled etching of the edges and corners of the nanocuboids provided additional geometric parameters to further fine-tune the plasmonic features of the nanoparticles. The longitudinal dipole plasmon peak was observed to progressively blue shift and become less intense as the edge and corner truncations proceeded. When a certain amount of Ag was removed from the nanocuboids after etching for ∼2 h, the ends of the Au nanorods became exposed and the longitudinal dipole plasmon resonance started to red-shift, accompanied by further decrease in peak intensity. The frequencies of the transverse plasmon modes, however, turned out to be much less sensitive to edge and corner truncations, and the transverse plasmon peaks became less distinguishable as their intensities gradually decreased during the etching process. After etching for ∼5 h, the longitudinal and transverse plasmonic features of the Au nanorods were both recovered, indicating complete etching of the Ag shell. Finite-difference time-domain (FDTD) calculations were performed to simulate the effects of the morphological changes on the plasmonic features of the nanoparticles at various stages during the etching process. As shown in Figure 1k, both the plasmon resonance frequencies and spectral line-shapes calculated by FDTD were in quantitative agreement with those in the experimental extinction spectra.

Cu^{2+}, AA, and CTAC all played crucial roles in this morphological evolution. No morphological or structural changes of the nanocuboids were observed when only Cu^{2+} (Supporting Information Figure S4) or AA (Supporting Information Figure S5) was present. Cu^{2+} and AA, which have been previously used for etching of Au nanorods,[40,41] were found to work synergistically as an effective etchant that oxidized metallic Ag under the current experimental conditions. The Ag^+ cations generated in situ combined with the Cl^- anions dissociated from CTAC to form AgCl microparticles (Supporting Information Figure S6), which could be subsequently removed by washing the etched samples with 100 mM CTAC due to the formation of soluble $AgCl_2^-$ complex. Although CTAC itself was apparently incapable of inducing any structural changes to the nanocuboids (Supporting Information Figure S7), it played key roles in preventing the nanoparticles from aggregation and selectively protecting

Ag {100} facets from etching. Etching of Au−Ag core−shell nanocuboids in the absence of CTAC resulted in the formation of large-scale aggregates composed of irregular particles. The Cu^{2+}/AA-induced etching of the nanocuboids in the presence of cetyltrimethylammonium bromide (CTAB) as the surface capping agent resulted in the formation of much less uniform, irregularly shaped nanoparticles (Supporting Information Figure S8) most likely due to the fact that CTAB provided weaker protection of the Ag {100} facets than CTAC and, thus, lacked the capability to guide the formation of the well-defined rice-shaped morphology.

A strikingly different facet-selective etching process was observed when the Au−Ag core−shell nanocuboids were exposed to Fe^{3+} in the presence of CTAB. As illustrated in Figure 2a, the morphological changes were dominated by the lateral etching of the Ag {100} facets on the sides of the nanocuboids, whereas the edge and corner truncations were observed to be significantly slower than the side facet indentation. This lateral side-facet etching resulted in the formation of dumbbell-shaped nanoparticles as shown in the SEM and TEM images in Figure 2b−g. The indentation from the side facets of the nanocuboids introduced dramatic changes to the plasmon resonance energies and overall extinction spectral line-shapes. As shown in Figure 2h, at the beginning stage of this lateral side-facet etching, the longitudinal dipole plasmon resonance slightly blue-shifted due to the increased degree of edge and corner truncations of the nanocuboids. As the etching proceeded, the side-facet etching became predominant, causing progressive red-shift of the longitudinal dipole plasmon resonance as the indentation of the side facets increased. The intensity of the longitudinal dipole plasmon peak gradually decreased as increasing amount of Ag was etched whereas, interestingly, the transverse plasmon peaks remained robust in intensity with only moderate blue-shifts in their resonance wavelengths. The effects of the side facet-etching on the plasmonic features of the nanoparticles were also simulated with FDTD (Figure 2i), which showed very good agreement with the experimental observations.

Fe^{3+} and CTAB were found to work synergistically in guiding the morphological evolution from the nanocuboids to the nanodumbbells. Fe^{3+} has been identified to be capable of oxidizing metallic Ag nanoparticles into ionic Ag^+.[42,43] No etching of the nanocuboids was observed when the particles were dispersed in CTAB in the absence of Fe^{3+} (Supporting Information Figure S9). During the etching process, submicrometer AgBr particles were identified as a major byproduct (see Supporting Information Figure S10), which could be completely removed by washing the etched samples with 100 mM CTAB upon the formation of soluble $AgBr_2^-$ complex. Though CTAB molecules form densely packed bilayers on the side facets of Au nanorods, the CTAB packing density on the Ag facets has been reported to be much lower than on the Au surfaces.[43] Therefore, in addition to the slow etching at the edges and corners of the nanocuboids, the lateral side facet etching became predominant due to the insufficient protection of the Ag {100} facets on the sides of the nanocuboids. Although cylindrical Au−Ag core−shell nanorods do not have well-defined surface facets, they have recently been observed to undergo a similar lateral etching process in the presence of Fe^{3+} and CTAB, which leads to the formation of Ag-tipped Au nanorods.[43] Using CTAC instead of CTAB as the capping ligand, the Fe^{3+}-induced etching of the nanocuboid side facets along the lateral direction was significantly slowed down
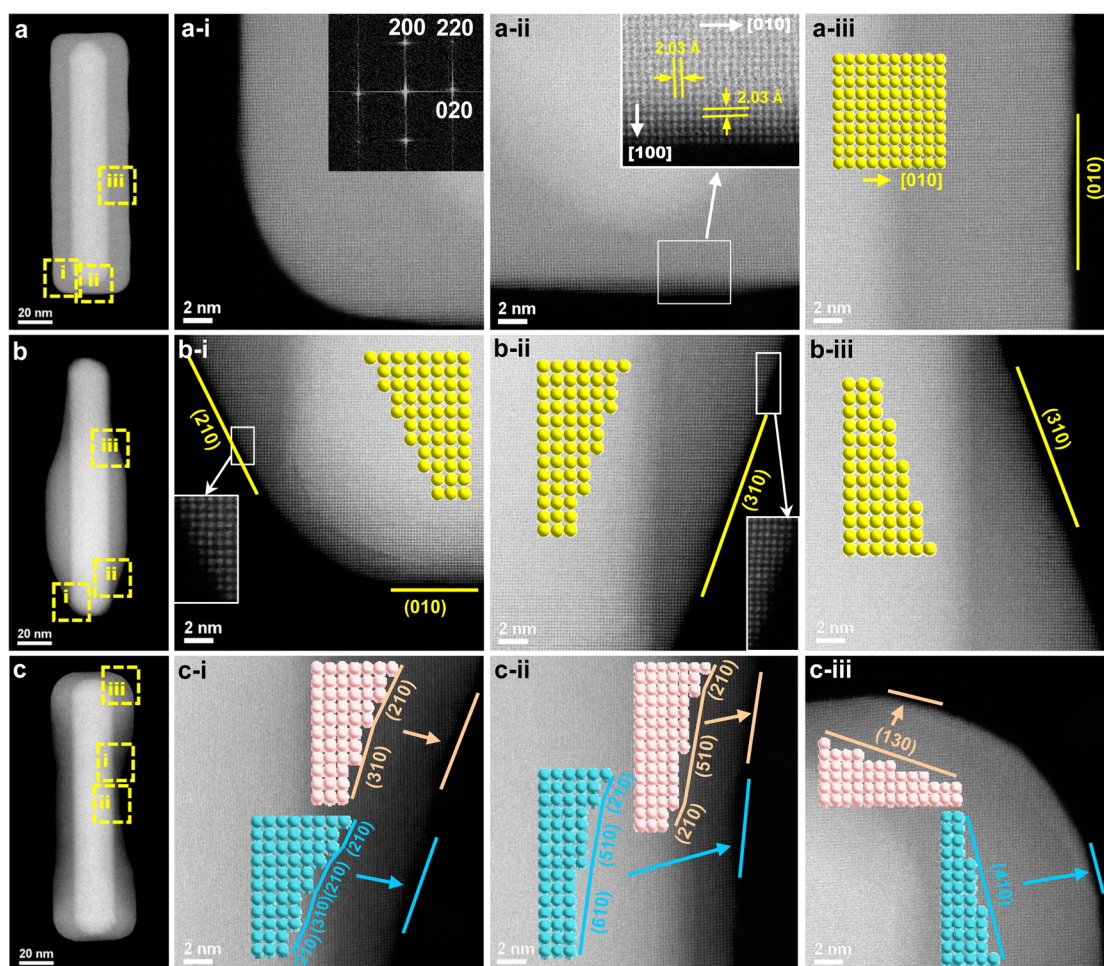
Figure 3. Atomic level surface structures of nanocuboid, nanorice, and nanodumbbell particles. HAADF-STEM images of individual Au−Ag core−shell (a) nanocuboid, (b) nanorice, and (c) nanodumbbell particles. The particles were imaged with projection from the [001] zone axis. (x-i, x-ii, x-iii, x = a, b, c) High-resolution HAADF-STEM images showing the atomic arrangements in three different regions (i, ii, and iii) for each nanostructure labeled in panels a, b, and c, respectively. The upper-right inset in panel a-i is the fast Fourier transform (FFT) pattern of the region shown in panel a-i. The regions encompassed by squares in panels a-ii, b-i, and b-ii are further zoomed in as the inset pictures in each panel. The schematics illustrating the atomic level structures of the corresponding low-index or high-index facets are shown in each panel.

(Supporting Information Figure S11) most likely due to the stronger protection of Ag {100} facets by CTAC than by CTAB.

The nanoscale surface etching of the Au−Ag core−shell nanocuboids provided a unique approach for the creation of high-index facets on nanoparticle surfaces. The atomic-level surface structures of the nanocuboid, nanorice, and nanodumbbell particles were resolved using high-angle annular dark-field scanning transmission electron microscopy (HAADF-STEM).[44−46] The HAADF-STEM images shown in Figure 3 were all taken with the electron beam projected along the [001] zone axis. Each nanoparticle was single-crystalline in nature, with the Au core and Ag shell both in the face-centered cubic (fcc) crystalline phase with lattice mismatch smaller than 0.25%. The epitaxial growth of Ag at the Au−Ag interfaces was clearly observed in the high-resolution HAADF-STEM images. The nanocuboid shown in Figure 3a-i−3a-iii was enclosed predominantly by {100} facets with some slight truncations at the edges and corners. As shown in Figure 3b-i−3b-iii, various well-defined high-index facets, such as {210} and {310} facets, were clearly resolved on the etched surfaces of the nanorice particles. Multiple stepped and kinked surfaces composed of various localized high-index facets, such as {310}, {410}, {510},

and {610}, were found at the tips and sides of the nanodumbbell particle (see Figure 3c-i−3c-iii). In striking contrast to small metal nanocrystals (less than 10 nm³ in volume) whose surface structures are unstable under intense electron beam illumination,[46] we found that the high-index facets on the nanorice and nanodumbbell particles were highly stable with no observable atomic level structural rearrangements under the electron beam illumination for more than 30 min. The geometric profiles of the nanoparticles, which were defined by the high-index facets exposed on particle surfaces, also appeared to be highly stable based on TEM characterizations and the detailed extinction spectral features of the nanoparticles were all well preserved (Supporting Information Figure S12) even after the colloidal particles were stored in water at room temperature for four months. The structural stability of the high-index facets on the etched nanoparticles may be interpreted as a result of the surface-stabilization effects of the surface-capping ligands, CTAC and CTAB.

The nanorice and nanodumbbell particles combined geometrically tunable plasmon resonances and catalytically active high-index facets, which allowed us to gain quantitative insights into the kinetics and mechanisms of nanoparticle-catalyzed reactions using time-resolved surface-enhanced Raman spec-
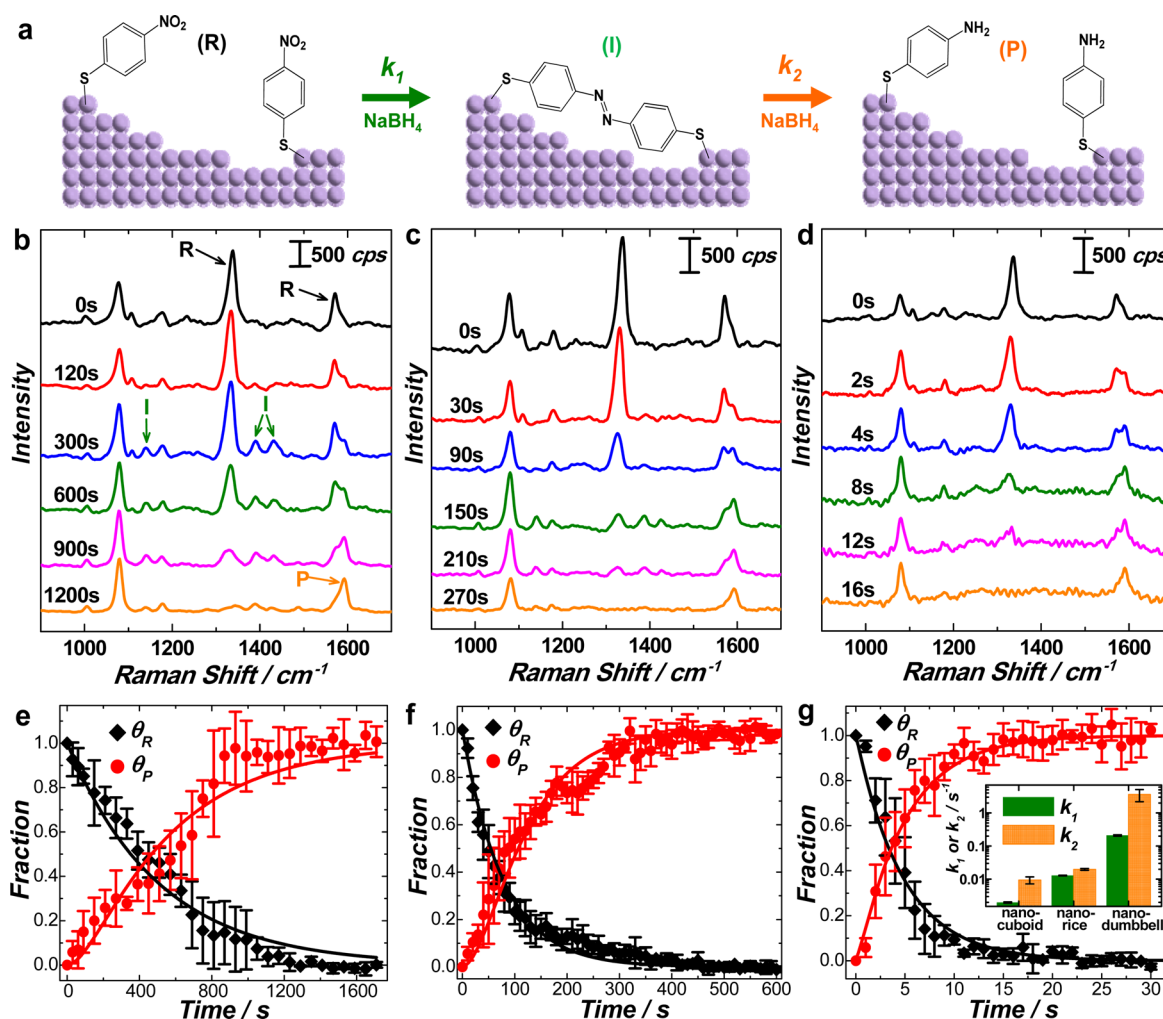
Figure 4. Catalytic activities of the nanocuboid, nanorice, and nanodumbbell particles. (a) Schematic illustration of the chemical reduction of surface-adsorbed 4-NTP (reactant, R) to DMAB (intermediate, I), and finally to 4-ATP (product, P) catalyzed by the nanoparticles. (b) SERS spectra collected from 4-NTP molecules adsorbed on the surfaces of nanocuboids at reaction times of 0, 120, 300, 600, 900, and 1200 s after adding $NaBH_4$. (c) SERS spectra collected from 4-NTP molecules adsorbed on the surfaces of nanorice particles at reaction times of 0, 30, 90, 150, 210, and 270 s after adding $NaBH_4$. (d) SERS spectra collected from 4-NTP molecules adsorbed on the surfaces of nanodumbbells at reaction times of 0, 2, 4, 8, 12, and 16 s after adding $NaBH_4$. Fraction of reactant (θ_R) and product (θ_P) as a function of reaction time during the reactions catalyzed by (e) nanocuboid, (f) nanorice, and (g) nanodumbbell particles. The error bars show the standard deviations obtained from five experimental runs. The results of least-squares fitting are shown as solid curves. The inset in panel g shows the comparison of rate constants (k_1 and k_2) of the two-step surface reactions on nanocuboid, nanorice, and nanodumbbell particles.

troscopy (SERS). The reduction of *p*-nitrophenol by $NaBH_4$ is a model reaction, which has been extensively investigated by UV−vis absorption spectroscopy, for the evaluation of catalytic activities of metallic nanoparticles in aqueous solutions.[47] Here, we systematically compared the catalytic activities of the nanocuboid, nanorice, and nanodumbbell particles using the reduction of preadsorbed 4-nitrothiophenol (4-NTP) by $NaBH_4$ as a model reaction. By measuring the SERS from the monolayer molecules preadsorbed on the surfaces of free-standing nanoparticles, we were able to study both the intrinsic reaction mechanisms and kinetics in real time without the complication introduced by the diffusion, adsorption, and desorption of reactants and products. In addition, the identification of transient intermediates during the surface-catalyzed reactions became possible. To prepare the samples for SERS measurements, colloidal suspensions of the nanoparticles were incubated with ethanolic solution of 4-NTP overnight to undergo a ligand exchange process thorough which saturated

self-assembled monolayers (SAMs) of 4-NTP on the nano-particle surfaces formed. Although SAMs of 4-NTP were assembled uniformly over the entire nanoparticle surfaces, the spectroscopic features were dominated by those molecules in the SERS "hot spots" where the local electric fields were significantly enhanced upon plasmonic excitation. FDTD calculations (Supporting Information Figure S13) showed that upon the excitation of the longitudinal dipole plasmon resonances, the near-field "hot-spots" for SERS were located in close proximity to the particle surfaces coincident with the high-index facets. Through careful geometry control during the etching processes, the longitudinal dipole plasmons of the nanocuboid, nanorice, and nanodumbbell particles were all tuned to be resonant with the excitation laser ($\lambda = 785$ nm) to achieve large SERS enhancements (Supporting Information Figure S14).

As illustrated in Figure 4a, the preadsorbed monolayer 4-NTP underwent a two-step reduction process to form the final

product, 4-aminothiophenol (4-ATP), upon exposure to NaBH$_4$. As shown in the SERS spectra (Figure 4b–d), 4-NTP has three characteristic vibrational Raman bands at 1076, 1338, and 1571 cm^{-1}, corresponding to C–S stretching, O–N–O stretching, and the phenol-ring modes, respectively.[33] As the reaction proceeded, the intensities of both 1338 and 1571 cm^{-1} bands decreased progressively with the concomitant emergence of a new band corresponding to the phenol-ring modes of 4-ATP at 1590 cm^{-1}.[48] All the vibrational modes observed in SERS correlate well with the bands in normal Raman spectra (Supporting Information Figure S15). The time-resolved SERS measurements also allowed us to identify 4,4′-dimercaptoazobenzene (DMAB), whose characteristic Raman modes are at 1140, 1388, and 1438 cm^{-1},[49,50] as the intermediate along the reaction pathway. We used a confocal Raman microscope for the SERS measurements with the laser beam focused into a small volume (∼100 pL) of the colloidal nanoparticle suspensions. In this confocal mode, each freely diffusing nanoparticle was exposed to the excitation laser for a short time period (within the diffusion time), which effectively eliminated the photoconversion of 4-NTP to DMAB.[48−50] The possibility of photoinduced formation of DMAB was ruled out by the control experiments in the absence of NaBH$_4$ (Supporting Information Figures S16 and S17).

The Raman modes at 1338 and 1590 cm^{-1} were used to quantify the fraction of reactant and product molecules, respectively, at various reaction times, based on which the reaction trajectories were obtained (Figure 4e−g). Under our experimental conditions, NaBH$_4$ (50 mM) was in excess and its concentration maintained constant throughout the whole reaction. Therefore, this surface reaction obeyed pseudo-first-order kinetics and the rate constants could be determined by performing least-squares curve fitting to the reaction trajectories shown in Figure 4e−g. The rate equations for this two-step consecutive reaction are listed as follows:

$$\theta_R = e^{-k_1 t}$$

$$\theta_P = 1 - \frac{1}{k_2 - k_1}(k_2 e^{-k_1 t} - k_1 e^{-k_2 t})$$

where θ_R and θ_P are the fractions of the 4-NTP and 4-ATP, respectively, k_1 and k_2 are the rate constants for the first and second steps, respectively, and t is the reaction time.

Both nanorice and nanodumbbells exhibited drastically enhanced catalytic activities in comparison to the nanocuboids due to the presence of high-index facets on the particle surfaces. Although the surface reactions may induce atomic rearrangements of Ag due to the relatively high mobility of Ag in comparison to Au, Pd, and Pt, TEM measurements (Supporting Information Figure S18) show that the overall morphologies of both the nanorice and nanodumbbell particles were well preserved during the reactions. As shown in the inset of Figure 4g, nanodumbbells exhibited the highest catalytic activity with k_1 approximately 10 times higher than for the nanorice particles and 2 orders of magnitude higher than for the nanocuboids. The nanodumbbells exhibited higher overall catalytic activities than the nanorice particles most likely due to the fact that the nanodumbbell surfaces were composed of high density of localized surface kinks, ledges, and steps whereas the nanorice particles had relatively flat surfaces enclosed by certain types of high index facets. The fraction of the intermediate, DMAB, was dependent on the relative ratios between k_1 and k_2.

Because k_2 was significantly larger than k_1 on all three nanostructures, the fraction of DMAB remained very small throughout the whole reaction processes, making it difficult to be identified. Interestingly, the vibrational bands of DMAB were clearly resolved in our time-resolved SERS measurements because of the high detection sensitivity of SERS and the fact that the Raman cross-section of DMAB is more than 3 orders of magnitude higher than that of the benzenethiol derivatives.[50] It is worth mentioning that the k_1 and k_2 values reported here were calculated based on the assumption that DMAB was the only intermediate along the two-step consecutive reaction pathway as illustrated in Figure 4a. The surface-catalyzed hydrogenation of 4-NTP, however, may be more complicated than described here and may involve other intermediates along alternative reaction pathways that are not readily resolvable by SERS. Therefore, k_1, which describes the consumption rate of the 4-NTP, should be generally used to evaluate the apparent reaction kinetics and relative catalytic activities of the nanoparticles, whereas k_2 may be further complicated if other reaction pathways coexist.

In summary, this work bridges two important fields: nanoplasmonics and nanocatalysis. We have demonstrated that creation of high-index facets on subwavelength metallic nanoparticles through controlled site-selective chemical etching provides a unique approach to the integration of tunable plasmon resonances and superior catalytic activities on the same nanoscale entity, which is both fundamentally of high interest and technically important. Tunable plasmonic nanostructures with catalytically active high-index facets represent a new class of materials with dual functionality that allows for the development of detailed, quantitative understanding of nanoparticle-catalyzed reactions through specifically designed plasmon-enhanced spectroscopic measurements. It is envisioned that tunable plasmonic nanostructures enclosed exclusively by certain types of well-defined high index facets provide unique materials systems that will enable us to gain further insights into the origin of the facet-dependent catalytic activity and selectivity of metallic nanoparticles.

■ EXPERIMENTAL DETAILS

Nanoparticle Synthesis. Au nanorods were fabricated using a recently published seed-mediated growth method.[36] Au−Ag core−shell nanocuboids were prepared through controlled epitaxial overgrowth of Ag on Au nanorods following a previous reported protocol[37] with some minor modifications. More experimental details about the fabrication of Au nanorods and Au−Ag core−shell nanocuboids are included in the Supporting Information.

The Au−Ag core−shell nanocuboids were centrifuged (5000 rpm, 5 min), washed with water once, and redispersed in 2 mL of solution consisting of 5 mM CTAC and 3.75 mM ascorbic acid (AA). The edge and corner etching was initiated upon the addition of 30 μL of 5 mM Cu(NO$_3$)$_2$ at 65 °C. For the lateral side facet etching, the Au−Ag nanocuboids were first centrifuged (5000 rpm, 5 min), then washed with water once, and finally redispersed in 2 mL of 5 mM CTAB solution. Then 50 μL of 50 mM Fe(NO$_3$)$_3$ was injected into the solution at 65 °C. UV−vis extinction spectra of the etched samples were recorded in real time to monitor the nanoscale surface etching processes. The etching processes were stopped at various reaction times by separating the etched nanoparticles from the reaction mixtures through centrifugation and redispersion in water. The byproducts, AgCl and AgBr, were removed by

washing the etched samples with 100 mM CTAC and CTAB, respectively. The etched nanostructures at certain etching stages were finally redispersed in water for detailed structural and spectroscopic characterizations.

Structural and Optical Characterizations. The morphologies and structures of the nanoparticles were characterized by TEM using a Hitachi H-8000 transmission electron microscope, which was operated at an accelerating voltage of 200 kV. All samples for TEM measurements were dispersed in water and drop-dried on 300 mesh Formvar/carbon-coated-Cu grids (Electron Microscopy Science Inc.). The structures and compositions of the nanoparticles were also characterized by SEM and EDS measurements using a Zeiss Ultraplus thermal field emission scanning electron microscope. The samples for SEM and EDS measurements were dispersed in water and drop-dried on silicon wafers. The atomic level structures of the nanoparticles were resolved by HAADF-STEM using a JEOL 2100F 200 kV FEG-STEM/TEM microscopy equipped with a CEOS CS corrector on the illumination system. The samples for HAADF-STEM measurements were dispersed in water and drop-dried on 400 mesh Cu grids with ultrathin carbon support film (Electron Microscopy Science Inc.). The optical extinction spectra of the nanoparticles were measured on aqueous colloidal suspensions at room temperature using a Beckman coulter Du 640 spectrophotometer.

FDTD Calculations. The far-field and near-field plasmonic properties of the nanoparticles were calculated using a commercial FDTD package (Lumerical Solutions). More details of FDTD calculations are included in the Supporting Information.

Time-Resolved SERS Measurements. Colloidal suspensions, each 25 μL in volume, of Au–Ag core–shell nanocuboid, nanorice, and nanodumbbell particles with roughly the same particle concentrations (~2 × 10^{10} particles mL^{-1}) were each incubated with 500 μL of ethanol solution of 1.0 mM 4-NTP overnight to form self-assembled monolayers of 4-NTP on the nanoparticles surfaces. Then the nanoparticles were centrifuged (5000 rpm, 5 min) and redispersed in 50 μL of ultrapure H$_2$O. The nanoparticle-catalyzed 4-NTP reduction occurred at room temperature upon the addition of 50 μL of 100 mM NaBH$_4$ in a 0.5 mL Eppendorf centrifuge tube. The kinetics of the catalyzed reactions was measured in real time using time-resolved SERS. SERS spectra were obtained on a Bayspec *Nomadic* confocal Raman microscopy built on an Olympus BX51 reflected optical system with a 785 nm continuous wave excitation laser. The excitation laser was focused on the reaction mixture using a 10× objective [numerical aperture (NA) = 0.30, working distance (WD) = 11.0 mm, Olympus MPLFLN]. The laser power was measured to be 3.6 mW at the samples and the signal acquisition times were 5 s for nanocuboid, 5 s for nanorice, and 1s for nanodumbbell particles, respectively. Successive SERS spectra were collected during the reaction until completion of the reduction of 4-NTP into 4-ATP. Normal Raman spectra were obtained on solid thin films of neat 4-NTP and 4-ATP on the silicon wafers under the same conditions.

ASSOCIATED CONTENT

Ⓢ Supporting Information
Additional experimental details, TEM and SEM images, size histograms, and EDS, extinction, Raman, and SERS spectra. This material is available free of charge via the Internet at http://pubs.acs.org.

AUTHOR INFORMATION

Corresponding Author
*H. Wang. E-mail: wang344@mailbox.sc.edu. Phone: 1-803-777-2203. Fax: 1-803-777-9521.

Notes
The authors declare no competing financial interest.

ACKNOWLEDGMENTS

REFERENCES

(1) Roduner, E. *Chem. Soc. Rev.* **2006**, *35*, 583−592.
(2) Astruc, D.; Lu, F.; Aranzaes, J. R. *Angew. Chem., Int. Ed.* **2005**, *44*, 7852−7872.
(3) Burda, C.; Chen, X. B.; Narayanan, R.; El-Sayed, M. A. *Chem. Rev.* **2005**, *105*, 1025−1102.
(4) Eustis, S.; El-Sayed, M. A. *Chem. Soc. Rev.* **2006**, *35*, 209−217.
(5) Liz-Marzan, L. M. *Langmuir* **2006**, *22*, 32−41.
(6) Valden, M.; Lai, X.; Goodman, D. W. *Science* **1998**, *281*, 1647−1650.
(7) Hvolbaek, B.; Janssens, T. V. W.; Clausen, B. S.; Falsig, H.; Christensen, C. H.; Norskov, J. K. *Nano Today* **2007**, *2*, 14−18.
(8) Janssens, T. V. W.; Clausen, B. S.; Hvolbaek, B.; Falsig, H.; Christensen, C. H.; Bligaard, T.; Norskov, J. K. *Top. Catal.* **2007**, *44*, 15−26.
(9) Halas, N. J.; Lal, S.; Chang, W. S.; Link, S.; Nordlander, P. *Chem. Rev.* **2011**, *111*, 3913−3961.
(10) Jain, P. K.; Huang, X. H.; El-Sayed, I. H.; El-Sayed, M. A. *Acc. Chem. Res.* **2008**, *41*, 1578−1586.
(11) Lal, S.; Link, S.; Halas, N. J. *Nat. Photonics* **2007**, *1*, 641−648.
(12) Knight, M. W.; Sobhani, H.; Nordlander, P.; Halas, N. J. *Science* **2011**, *332*, 702−704.
(13) Ferry, V. E.; Munday, J. N.; Atwater, H. A. *Adv. Mater.* **2010**, *22*, 4794−4808.
(14) Willets, K. A.; Van Duyne, R. P. *Annu. Rev. Phys. Chem.* **2007**, 267−297.
(15) Giljohann, D. A.; Seferos, D. S.; Daniel, W. L.; Massich, M. D.; Patel, P. C.; Mirkin, C. A. *Angew. Chem., Int. Ed.* **2010**, *49*, 3280−3294.
(16) Scholl, J. A.; Koh, A. L.; Dionne, J. A. *Nature* **2012**, *483*, 421−U68.
(17) Tian, N.; Zhou, Z. Y.; Sun, S. G.; Ding, Y.; Wang, Z. L. *Science* **2007**, *316*, 732−735.
(18) Quan, Z. W.; Wang, Y. X.; Fang, J. Y. *Acc. Chem. Res.* **2013**, *46*, 191−202.
(19) Rycenga, M.; Cobley, C. M.; Zeng, J.; Li, W. Y.; Moran, C. H.; Zhang, Q.; Qin, D.; Xia, Y. N. *Chem. Rev.* **2011**, *111*, 3669−3712.
(20) Ahmadi, T. S.; Wang, Z. L.; Green, T. C.; Henglein, A.; ElSayed, M. A. *Science* **1996**, *272*, 1924−1926.
(21) Sun, Y. G.; Xia, Y. N. *Science* **2002**, *298*, 2176−2179.
(22) Ming, T.; Feng, W.; Tang, Q.; Wang, F.; Sun, L. D.; Wang, J. F.; Yan, C. H. *J. Am. Chem. Soc.* **2009**, *131*, 16350−16351.
(23) Zhang, J.; Langille, M. R.; Personick, M. L.; Zhang, K.; Li, S. Y.; Mirkin, C. A. *J. Am. Chem. Soc.* **2010**, *132*, 14012−14014.
(24) Tran, T. T.; Lu, X. M. *J. Phys. Chem. C* **2011**, *115*, 3638−3645.

(25) Ma, Y. Y.; Kuang, Q.; Jiang, Z. Y.; Xie, Z. X.; Huang, R. B.; Zheng, L. S. *Angew. Chem., Int. Ed.* **2008**, *47*, 8901−8904.

(26) Yu, T.; Kim, D. Y.; Zhang, H.; Xia, Y. N. *Angew. Chem., Int. Ed.* **2011**, *50*, 2773−2777.

(27) Zhou, Z. Y.; Huang, Z. Z.; Chen, D. J.; Wang, Q.; Tian, N.; Sun, S. G. *Angew. Chem., Int. Ed.* **2010**, *49*, 411−414.

(28) Huang, X. Q.; Zhao, Z. P.; Fan, J. M.; Tan, Y. M.; Zheng, N. F. *J. Am. Chem. Soc.* **2011**, *133*, 4718−4721.

(29) Tian, N.; Zhou, Z. Y.; Yu, N. F.; Wang, L. Y.; Sun, S. G. *J. Am. Chem. Soc.* **2010**, *132*, 7580−7581.

(30) Jin, M. S.; Zhang, H.; Xie, Z. X.; Xia, Y. N. *Angew. Chem., Int. Ed.* **2011**, *50*, 7850−7854.

(31) Yu, Y.; Zhang, Q. B.; Liu, B.; Lee, J. Y. *J. Am. Chem. Soc.* **2010**, *132*, 18258−18265.

(32) Wang, F.; Li, C. H.; Sun, L. D.; Wu, H. S.; Ming, T. A.; Wang, J. F.; Yu, J. C.; Yan, C. H. *J. Am. Chem. Soc.* **2011**, *133*, 1106−1111.

(33) Huang, J. F.; Zhu, Y. H.; Lin, M.; Wang, Q. X.; Zhao, L.; Yang, Y.; Yao, K. X.; Han, Y. *J. Am. Chem. Soc.* **2013**, *135*, 8552−8561.

(34) Zhang, L.; Zhang, J. W.; Kuang, Q.; Xie, S. F.; Jiang, Z. Y.; Xie, Z. X.; Zheng, L. S. *J. Am. Chem. Soc.* **2011**, *133*, 17114−17117.

(35) Xia, X. H.; Zeng, J.; McDearmon, B.; Zheng, Y. Q.; Li, Q. G.; Xia, Y. N. *Angew. Chem., Int. Ed.* **2011**, *50*, 12542−12546.

(36) Ye, X. C.; Zheng, C.; Chen, J.; Gao, Y. Z.; Murray, C. B. *Nano Lett.* **2013**, *13*, 765−771.

(37) Jiang, R. B.; Chen, H. J.; Shao, L.; Li, Q.; Wang, J. F. *Adv. Mater.* **2012**, *24*, OP200−OP207.

(38) Okuno, Y.; Nishioka, K.; Kiya, A.; Nakashima, N.; Ishibashi, A.; Niidome, Y. *Nanoscale* **2010**, *2*, 1489−1493.

(39) Li, Q.; Jiang, R. B.; Ming, T.; Fang, C. H.; Wang, J. F. *Nanoscale* **2012**, *4*, 7070−7077.

(40) Sreeprasad, T. S.; Samal, A. K.; Pradeep, T. *Langmuir* **2007**, *23*, 9463−9471.

(41) Wen, T.; Zhang, H.; Tang, X. P.; Chu, W. G.; Liu, W. Q.; Ji, Y. L.; Hu, Z. J.; Hou, S.; Hu, X. N.; Wu, X. C. *J. Phys. Chem. C* **2013**, *117*, 25769−25777.

(42) Cobley, C. M.; Rycenga, M.; Zhou, F.; Li, Z. Y.; Xia, Y. N. *J. Phys. Chem. C* **2009**, *113*, 16975−16982.

(43) Guo, X.; Zhang, Q.; Sun, Y. H.; Zhao, Q.; Yang, J. *ACS Nano* **2012**, *6*, 1165−1175.

(44) Goris, B.; De Backer, A.; Van Aert, S.; Gomez-Grana, S.; Liz-Marzan, L. M.; Van Tendeloo, G.; Bals, S. *Nano Lett.* **2013**, *13*, 4236−4241.

(45) Katz-Boon, H.; Rossouw, C. J.; Weyland, M.; Funston, A. M.; Mulvaney, P.; Etheridge, J. *Nano Lett.* **2011**, *11*, 273−278.

(46) Li, Z. Y.; Young, N. P.; Di Vece, M.; Palomba, S.; Palmer, R. E.; Bleloch, A. L.; Curley, B. C.; Johnston, R. L.; Jiang, J.; Yuan, J. *Nature* **2008**, *451*, 46−48.

(47) Herves, P.; Perez-Lorenzo, M.; Liz-Marzan, L. M.; Dzubiella, J.; Lu, Y.; Ballauff, M. *Chem. Soc. Rev.* **2012**, *41*, 5577−5587.

(48) Huang, Y. F.; Zhu, H. P.; Liu, G. K.; Wu, D. Y.; Ren, B.; Tian, Z. Q. *J. Am. Chem. Soc.* **2010**, *132*, 9244−9246.

(49) Dong, B.; Fang, Y. R.; Chen, X. W.; Xu, H. X.; Sun, M. T. *Langmuir* **2011**, *27*, 10677−10682.

(50) Huang, Y. F.; Wu, D. Y.; Zhu, H. P.; Zhao, L. B.; Liu, G. K.; Ren, B.; Tian, Z. Q. *Phys. Chem. Chem. Phys.* **2012**, *14*, 8485−8497.